

Interface Amorphization — Driven Fracture Toughness Improvement and Charge Redistribution for Dendrite Suppression

Yiwei You,[§] Dexin Zhang,[§] Yan Liu, Xinrui Cao, Tie-Yu Lü, Yang Sun, Zi-Zhong Zhu, and Shunqing Wu*



Cite This: *ACS Appl. Mater. Interfaces* 2025, 17, 32163–32169



Read Online

ACCESS |



Metrics & More



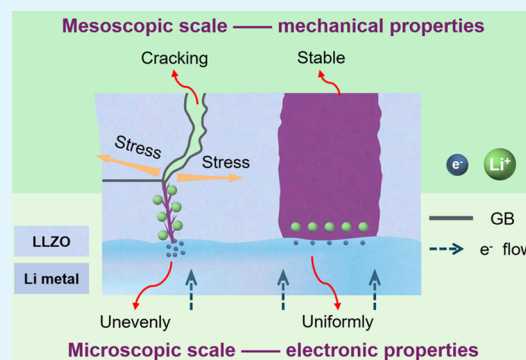
Article Recommendations



Supporting Information

ABSTRACT: All-solid-state batteries offer improved safety and energy density for vehicle electrification. Among various solid-state electrolytes, cubic garnet-type ceramic $\text{Li}_7\text{La}_3\text{Zr}_2\text{O}_{12}$ (LLZO) stands out due to its superior room-temperature ionic conductivity and chemical stability. However, challenges such as lithium dendrite formation persist, particularly along the interface and grain boundaries in LLZO. This study illustrates a method to enhance the stability of all-solid-state batteries by interfacial amorphization. Through computational modeling, we demonstrate that amorphous regions exhibit lower electron capture ability compared to interfaces, effectively suppressing lithium dendrite growth. In addition, compared with the interface structure, the structure without interface exhibits excellent mechanical properties, with higher energy requirements for fracture, enhancing resistance to crack propagation during charging/discharging cycles. In summary, we established a computational model from micro to mesoscopic scales, illustrating that interface amorphization can effectively enhance interface stability, which provides insights into interface issues in all-solid-state lithium metal batteries.

KEYWORDS: LLZO, amorphization, lithium dendrite, interfacial stability, mechanical properties



1. INTRODUCTION

All-solid-state batteries (ASSBs) represent the next generation of Li-ion batteries, crucial for advancing vehicle electrification. Unlike traditional liquid electrolytes, ASSBs utilize solid-state electrolytes, offering superior thermal stability and addressing safety and energy density concerns associated with Li-ion batteries.^{1–3} Among various solid-state electrolytes, cubic garnet-type ceramic $\text{Li}_7\text{La}_3\text{Zr}_2\text{O}_{12}$ (c-LLZO) stands out due to its high room-temperature ionic conductivity, chemical stability against Li metal, and wide electrochemical window.^{4–6} In a series of works,^{7,8} despite achieving a high relative density of 99.0% and ionic conductivity of 1.18 mS/cm², short-circuits persisted at a low current density of 0.8 mA/cm².

The growth of lithium dendrites is one of the main scientific issues in electrochemistry.⁹ In polycrystalline LLZO, research reveals the growth of lithium dendrites and whiskers, particularly along grain boundaries,^{10,11} attributed to high electronic conductivity, low ionic conductivity, and relatively low shear modulus.^{12–14} Interconnected pores and pre-existing cracks in the microstructure further facilitate lithium dendrite formation. Conversely, amorphous LLZO thin films, devoid of grain boundaries, inhibit lithium dendrite formation on electrodes. Sastre et al.¹⁵ successfully deposited grain-boundary-free amorphous LLZO onto crystalline LLZO, enhancing critical current density up to 3.2 mA/cm².

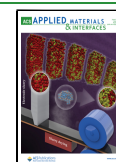
Amorphous intergranular films have been recognized as an effective strategy for enhancing the mechanical and electrochemical stability of solid-state electrolytes.¹⁶ This concept dates back to 1960, when Klement first observed the formation of amorphous structures in gold–silicon alloys. Since then, annealing-induced recrystallization has been found in an increasing number of amorphous alloys, such as Fe–P–C.¹⁷ The presence of nanocrystals in these amorphous alloys improves their properties, such as hardness and corrosion resistance, to a certain extent.¹⁸ Recent research indicates that solid-state electrolytes featuring amorphous–crystalline composite structures demonstrate enhanced ionic conductivity compared to their purely amorphous counterparts. This phenomenon is observed in various materials, such as microcrystalline glass sulfide-type solid-state electrolytes and composite polymer electrolytes.^{19–22} The synergistic effects between the amorphous and crystalline phases play a significant role in facilitating rapid Li-ion transport within these composite materials, with interfacial regions providing

Received: January 5, 2025

Revised: May 2, 2025

Accepted: May 19, 2025

Published: May 22, 2025



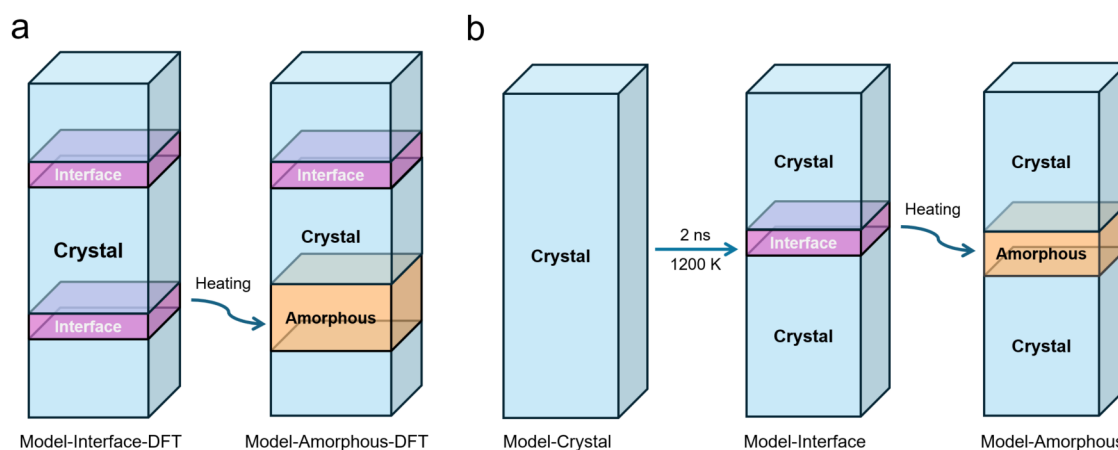


Figure 1. (a) Computational model for DFT calculations (~ 800 atoms) and (b) computational model for DPMD calculations ($\sim 30,000$ atoms).

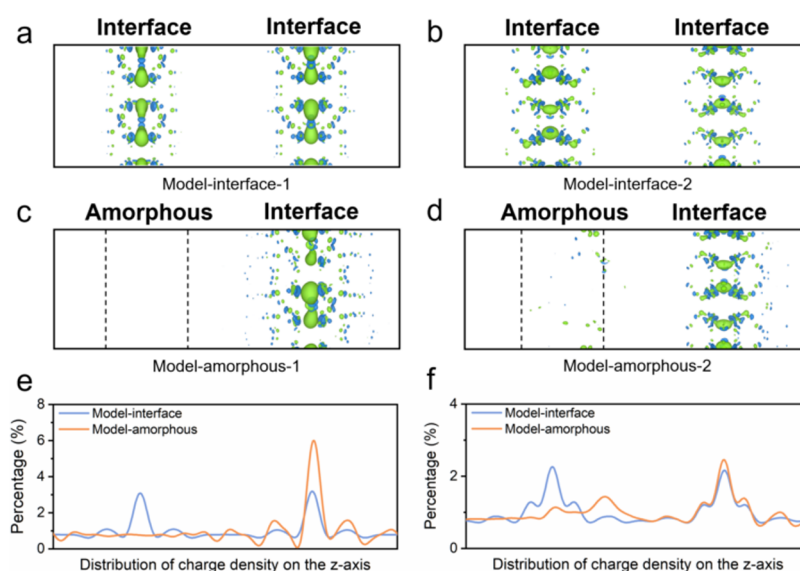


Figure 2. Distribution of excess charge in (a) Model-interface-1, (b) Model-interface-2, (c) Model-amorphous-1, (d) Model-amorphous-2. Distribution of excess charge along the z -axis in (e) Model-1 and (f) Model-2. Green represents positive charge density and blue represents negative charge density.

efficient ion transport pathways.^{23,24} Moreover, when the amorphous and crystalline phases share the same chemical composition, resulting in LLZO composite thin films, they exhibit isomeric characteristics. This property helps prevent potential elemental segregation and side reactions at the interface during the heat treatment process, contributing to the stability and performance of the electrolyte material.²⁵

Combining amorphous LLZO with c-LLZO to form microcrystalline glass can effectively suppress lithium dendrite formation while preserving ionic conductivity. Because the grain boundaries of LLZO are less stable than the bulk phase, localized heating techniques such as Joule heating^{26–30} can be used to selectively melt these regions. By precisely controlling the heating duration, it is possible to form crystalline–amorphous composite structures that eliminate grain boundaries while preserving the overall crystal integrity. This approach will hopefully address existing challenges encountered by LLZO.

This study aims to elucidate how grain boundary amorphization suppresses lithium dendrite formation and enhances interfacial stability, considering electronic and

mechanical perspectives across microscopic to mesoscopic scales. Figure 1a illustrates the structural model for computing electronic properties, while Figure 1b depicts the model used for calculating mechanical properties.

2. RESULTS

A large amount of charge will appear at the interface of LLZO and Li, and defects and other problems will also lead to excess charge. For this reason, we intend to study the ability of different models to capture excess charge.^{31–33} A cubic LLZO crystal was constructed and mirrored along the (110) plane, with Zr and La atoms as the central reference points. This process created a periodic structure with two grain boundaries. The details of these structures are shown in Supporting Figure 1 and Note 1. One of the GBs in the model melted into a 15 Å amorphous region by heating. Density functional theory (DFT) calculations were then performed to determine the distribution of excess charge in the Model-interface and Model-amorphous regions when the system contains excess charge. This computational approach has been proven accurate in previous works.^{31,34} Model-2 in Figure 2 was derived

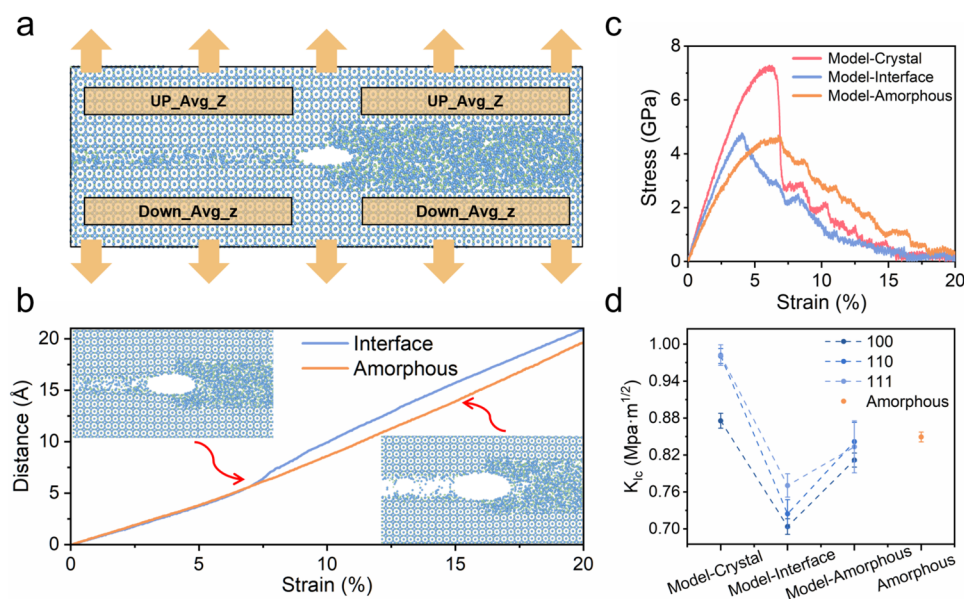


Figure 3. (a) Structural model for crack propagation simulation ($\sim 120,000$ atoms), (b) relationship between interlayer spacing and strain intensity, (c) tensile stress–strain curves for different systems, and (d) critical stress intensity factors for different systems.

similarly to Model-1, with the only distinction being the interfacial composition, demonstrating the generality of our findings.

The isosurface threshold was chosen to clearly highlight regions of relatively high electron density accumulation while suppressing background noise, and it was kept consistent across comparable figures. The isosurface value is set as $0.0003 \text{ e}/\text{\AA}^3$. As shown in Figure 2a,b, the excess charge in the system tends to accumulate at the grain boundary region. The elemental distribution and initial charge density of the model in Figure 2a are provided in Supporting Figures 2 and 3. It can be observed that the oxygen concentration at the grain boundary is lower than in the surrounding regions. This oxygen deficiency leads to a reduced initial charge density at the interface, which in turn promotes the localization of excess electrons in these regions. After amorphizing one of the interfaces and recalculating the distribution of excess charges, it was observed that the excess charges originally in the amorphous region concentrated on the interface side, as confirmed by Figure 2e,f. The amount of excess charge in the amorphous was close to the bulk level, while the amount of excess charge at the interface increased compared to the initial state. This conclusion indicates that the charge-trapping ability of the amorphous is significantly lower than that of the interface. Previously published work has shown that the uneven charge density distribution at the LLZO/Li interface can lead to uneven Li insertion, which easily forms lithium dendrites.³¹ Therefore, interfacial amorphization can effectively suppress lithium dendrite growth.

During the initial reduction of lithium metal at the LLZO/anode interface, internal stress is generated, and lithium dendrites tend to grow along the grain boundaries. As lithium dendrites grow along grain boundaries, they further generate stress, which can contribute to crack nucleation and propagation. To better understand the mechanical response of interfaces and amorphous regions under stress, we designed a model ($\sim 120,000$ atoms) containing an interface, an amorphous region, and a pre-existing crack, as shown in Figure 3a. The left side represents the interface region and the

right side depicts the amorphous region. Uniaxial tensile strain was applied along the z -axis at a constant rate to observe crack propagation. No atoms were frozen during the deformation. The simulation cell size was approximately $38.9 \times 350.2 \times 103.2 \text{ \AA}^3$, and the structure was uniformly deformed. The overall velocity drift was removed to eliminate artificial motion. The average displacements of all atoms within the box in Figure 3a were statistically analyzed, as depicted in Figure 3b, indicates a sudden change in the average displacement of interfacial atoms at a strain of 7.5%. At a strain of 15%, a noticeable crack emerges at the interface, while the amorphous structure remains relatively intact. This phenomenon indicates that the amorphous region is more effective in suppressing crack propagation compared to the interface.

We also verified the accuracy of the interatomic potential for calculating mechanical properties, with the computational model shown in Figure 1b. We performed uniaxial tensile tests along the (100), (110), and (111) directions of crystalline LLZO and compared the Young's moduli with previous DFT data, summarized in Table 1. Our interatomic potential demonstrated high accuracy in simulating Young's module along these three directions, exhibiting good agreement with the DFT data.

Table 1. Comparison of Moduli with Other DFT Data

structure	E100 (GPa)	E110 (GPa)	E111 (GPa)
Al-doped LLZO ³⁵	136.76	158.36	167.15
Ta-doped LLZO ³⁵	128.11	151.38	161.14
Pure LLZO ¹³	132.91	159.86	171.45
DPMD (this work)	133.15 ± 0.91	162.48 ± 1.88	171.06 ± 1.26

Subsequently, we simulated the stress–strain relationship of three models: Model-Crystal, Model-Interface, and Model-Amorphous, as shown in Figure 1b. Stress–strain relationships, depicted in Figure 3c for the (111) direction, revealed that all samples initially exhibited elastic deformation, with stress increasing with strain. However, significant differences emerged during subsequent stages. In the Model-Crystal

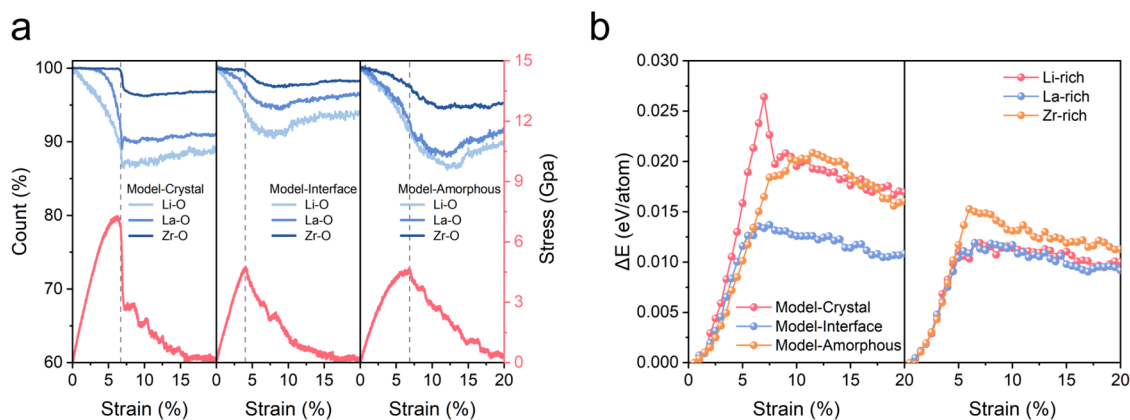


Figure 4. (a) Changes in the number of Li–O, La–O, and Zr–O bonds relative to the initial structure during the tensile process and (b) changes in energy relative to the initial energy during the tensile process for different systems and interfacial models. ΔE represents the change in average energy per atom after applying strain to the system.

system, rapid crack propagation ensued after elastic deformation, leading to complete fracture. In contrast, in the Model-Interface system, cracks began to propagate at lower strains due to the presence of the interface. Notably, the Model-Amorphous system exhibited a relatively long plastic deformation process after elastic deformation, and during crack propagation, substantial stress remained, hindering further crack extension effectively.

The critical stress intensity factor (K_{Ic}) can quantify a material's ability to suppress crack propagation, allowing for performance comparisons between different materials.³⁶ We calculated the K_{Ic} for the different samples and plotted them in Figure 3d. It was observed that the Model-Crystal system had the highest fracture toughness, which decreased significantly when a Model-Interface system with grain boundaries was formed. Notably, by melting the grain boundaries to form an amorphous structure and preparing a Model-Amorphous system, the fracture toughness increased by 15%, indicating that the Model-Amorphous system has better fracture resistance than the Model-Interface system.

To delve deeper into the structural changes during crack propagation, we conducted a statistical analysis of the variations in the number of Li–O, La–O, and Zr–O bonds relative to the initial structure within the fracture region during the tensile process, as illustrated in Figure 4a. In our bond analysis, we determine bond breakage based on the first minimum of the radial distribution function (RDF) for each specific pair of elements. A bond is considered broken when the interatomic distance exceeds this threshold. In the Model-Crystal, we observed a rapid decrease in the number of Li–O bonds with increasing tensile strain, attributed to the relatively weak bonds formed between Li and O due to Li's role as a migratory ion. Conversely, the La–O and Zr–O polyhedra, constituting the primary structural framework, exhibited stronger interactions. Notably, the number of Zr–O bonds remained nearly constant during the elastic deformation stage, while significant changes occurred in the La–O bonds. At approximately 6.8% strain, the Zr–O bonds lost stability, leading to substantial bond breaking and crack formation. In the Model-Interface system, due to the presence of interfacial defects, the Zr–O polyhedra at the interface became unstable, resulting in bond breaking at a strain of around 4%. However, in the Model-Amorphous system, although the number of all three types of bonds decreases during the elastic deformation

stage, bond rupture occurs only at a strain of about 6.8% (similar to Model-Crystal). The reduction in bond numbers in the amorphous region is not necessarily due to direct bond breakage but is more likely attributed to bond switching and local structural rearrangements, which are typical deformation mechanisms in amorphous oxides. During the elastic deformation stage, bonds are stretched but not broken, with real bond breakage occurring only when the strain reaches around 6.8%. The model-amorphous system exhibits better mechanical stability during crack propagation.

Figure 4b illustrates the changes in energy relative to the initial energy during the tensile process. It is evident that the Model-Crystal system necessitates the highest energy for fracture, indicative of its robust ability to suppress crack propagation, followed by the Model-Amorphous system. Conversely, the Model-Interface system requires the lowest energy for fracture, indicating poorer crack suppression ability. Given that the Zr–O interaction is the strongest, we constructed three different interfacial models to evaluate the enhancement in the energy required for fracture, as shown in Figure 4b. Results revealed that higher Zr content in the interface led to increased energy required for fracture.

3. CONCLUSIONS

Solid-state lithium batteries offer promising solutions for safer and more efficient power storage, with garnet-type LLZO electrolytes emerging as a key component. However, challenges related to grain boundaries and lithium dendrite growth hinder their widespread adoption. Our manuscript focuses on addressing these challenges through advanced methodologies, shedding light on LLZO electrolyte behavior.

At the microscopic scale, in the LLZO interface model, studies have shown that the amorphous region exhibits poor electron capture capabilities compared with the interface. Therefore, converting all LLZO interfaces into amorphous LLZO can significantly reduce the ability of LLZO to capture electrons, achieve uniform Li plating, and thereby inhibit the growth of lithium dendrites.

At the mesoscopic scale, Model-Amorphous systems exhibit excellent mechanical properties compared to Model-Interface system. The higher energy required to fracture the Model-Amorphous system enhances its resistance to crack propagation, thereby improving mechanical stability during charge/discharge cycles. At the same time, more stable mechanical

properties can effectively limit the further growth of lithium dendrites.

Overall, this study highlights the advantages of interfacial amorphization in forming microcrystalline LLZO in terms of both electronic and mechanical aspects, ultimately leading to enhanced interfacial stability.

4. METHODS

4.1. First-Principles Calculations. We performed first-principles calculations using the Vienna ab initio Simulation Package (VASP).^{37,38} The projector augmented wave (PAW) method³⁹ was employed in the calculations. The exchange-correlation functional used the spin-polarized generalized gradient approximation (GGA) parametrized by Perdew–Burke–Ernzerhof (PBE).⁴⁰ The chosen cutoff energy was 500 eV. The convergence criteria for energy and force were set to 10^{-4} eV and 0.1 eV/Å, respectively. In our calculations, only the Γ point in the Brillouin zone is used for k-point sampling. An excess electron was added to the system to investigate its charge distribution. A uniform background charge was applied to compensate for the added charge under periodic boundary conditions.^{31,41,42} Since our analysis focuses on qualitative trends rather than total energies, the impact of periodic artifacts is expected to be minimal.

4.2. Dynamics Simulation Calculations. The interatomic interactions were described using a DPMD-type potential,⁴³ whose accuracy has been verified in our previous work.^{44,45} The cutoff distance for the potential was set to 6 Å, and the resulting energy and force errors were within 10 meV/atom. The large-scale atomic/molecular massively parallel simulator (LAMMPS)⁴⁶ was used to perform the molecular dynamics (MD) simulations. To induce interfacial amorphization, the selected region was first heated to 3000 K, melted for 50 ps, and then slowly cooled to room temperature to form a structurally reasonable amorphous interface in the Model-Amorphous system. For the amorphous model, we heat up the entire material. All simulations related to mechanical properties in this study were conducted at 300 K.

4.3. Model in Figure 2. A cubic LLZO crystal was constructed and mirrored along the (110) plane, with Zr and La atoms as the central reference points. This process created a periodic structure with two grain boundaries. The structure was then relaxed using MD simulations to achieve stability. Additionally, the interface was heated, melted, and subsequently cooled to room temperature to form the amorphous structure. The final structure was further optimized using Density Functional Theory before performing electronic property calculations.

4.4. Model in Figure 3. First, a model with an ordered interface was constructed. The designated region was then heated and melted, followed by cooling to form a half-amorphous, half-interface structure. A pre-existing crack was introduced by removing atoms in the z-axis midpoint (1/2) within a defined elliptical region satisfying the equation: $\left(\frac{y}{10}\right)^2 + \left(\frac{z}{5}\right)^2 < 1$. To simulate mechanical response, tensile strain was applied to the top and bottom surfaces of the model at a strain rate of 0.0005/fs.

4.5. Model in Figure 4. The interface in the model corresponds to the (111) crystallographic orientations. We have constructed three different interfaces by selecting different elements as the symmetry axis, leading to Li-enriched, La-enriched, and Zr-enriched interfaces, respectively.

4.6. Critical Stress Intensity Factor. Fracture toughness is defined as the ability of a material to resist the propagation of cracks, which is typically characterized by the critical energy release rate (G_c). G_c is defined as the critical value of the stored strain energy released per unit crack area at the instant of fracture.⁴⁷ This critical value represents the maximum energy the material can withstand during crack propagation and is a key indicator of fracture toughness. The critical energy release rate can be calculated using the following formula.^{48,49}

$$G_c = \frac{1}{A_{\text{crack}}} \int F dl = \frac{V}{A_{\text{crack}}} \int \sigma d\varepsilon \quad (1)$$

Here, V is the initial volume, A_{crack} is the total crack area, σ and ε are the stress and strain along the tensile direction.

The critical stress intensity factor (K_{Ic}) is an important parameter widely used in the fields of materials mechanics and fracture mechanics to evaluate a material's ability to resist fracture in the presence of cracks. This parameter is related to the G_c , and K_{Ic} can be calculated from G_c .³⁶

$$K_{Ic} = \sqrt{G_c E'} = \sqrt{\frac{G_c E}{(1 - \mu^2)}} \quad (2)$$

where, E is the Young's modulus, obtained from the slope of the stress–strain curve during the elastic deformation stage under uniaxial tension. μ is the Poisson's ratio, obtained from the ratio of the deformation along the tensile direction to the deformation perpendicular to the tensile direction during the elastic deformation process.

■ ASSOCIATED CONTENT

Supporting Information

The Supporting Information is available free of charge at <https://pubs.acs.org/doi/10.1021/acsami.5c00248>.

Supporting Notes 1 and 2; structure of (a) Model-interface-1; (b) Model-interface-2; (c) Model-amorphous-1; (d) Model-amorphous-2 (Figure S1); elemental distribution along the horizontal axis within 2 Å intervals (Figure S2); original charge distribution (Figure S3); tensile stress-strain curves for amorphous (Figure S4); model-amorphous structure (Figure S5); tensile stress-strain curves for model-amorphous structure (Figure S6); data in Figure 3d (Table S1); Poisson ratios (Table S2) (PDF)

■ AUTHOR INFORMATION

Corresponding Author

Shunqing Wu – Department of Physics, OSED, Key Laboratory of Low Dimensional Condensed Matter Physics (Department of Education of Fujian Province), Xiamen University, Xiamen 361005, China; orcid.org/0000-0002-2545-0054; Email: wsq@xmu.edu.cn

Authors

Yiwei You – Department of Physics, OSED, Key Laboratory of Low Dimensional Condensed Matter Physics (Department of Education of Fujian Province), Xiamen University, Xiamen 361005, China; orcid.org/0000-0003-0022-4613

Dexin Zhang – Department of Physics, OSED, Key Laboratory of Low Dimensional Condensed Matter Physics (Department of Education of Fujian Province), Xiamen University, Xiamen 361005, China

Yan Liu – Department of Physics, OSED, Key Laboratory of Low Dimensional Condensed Matter Physics (Department of Education of Fujian Province), Xiamen University, Xiamen 361005, China; Yunnan Dianneng Smart Energy Co., Ltd, Kunming 650228 Yunnan, China

Xinrui Cao – Department of Physics, OSED, Key Laboratory of Low Dimensional Condensed Matter Physics (Department of Education of Fujian Province), Xiamen University, Xiamen 361005, China; orcid.org/0000-0002-2998-8863

Tie-Yu Lü – Department of Physics, OSED, Key Laboratory of Low Dimensional Condensed Matter Physics (Department of

Education of Fujian Province), Xiamen University, Xiamen 361005, China; orcid.org/0000-0002-9402-370X

Yang Sun – Department of Physics, OSED, Key Laboratory of Low Dimensional Condensed Matter Physics (Department of Education of Fujian Province), Xiamen University, Xiamen 361005, China; orcid.org/0000-0002-4344-2920

Zi-Zhong Zhu – Department of Physics, OSED, Key Laboratory of Low Dimensional Condensed Matter Physics (Department of Education of Fujian Province), Xiamen University, Xiamen 361005, China; orcid.org/0000-0001-5353-4418

Complete contact information is available at:
<https://pubs.acs.org/10.1021/acsami.5c00248>

Author Contributions

§Y.Y. and D.Z. contributed equally to this work.

Notes

The authors declare no competing financial interest.

ACKNOWLEDGMENTS

This research was supported by the National Natural Science Foundation of China (Nos. 11874307 and T2422016). Shaorong Fang and Tianfu Wu from the Information and Network Center of Xiamen University are acknowledged for their help with the Graphics Processing Unit (GPU) computing.

REFERENCES

- (1) Janek, J.; Zeier, W. G. A solid future for battery development. *Nat. Energy* **2016**, *1* (9), No. 16141.
- (2) Hatzell, K. B.; Chen, X. C.; Cobb, C. L.; Dasgupta, N. P.; Dixit, M. B.; Marbella, L. E.; McDowell, M. T.; Mukherjee, P. P.; Verma, A.; Viswanathan, V.; et al. Challenges in Lithium Metal Anodes for Solid-State Batteries. *ACS Energy Lett.* **2020**, *5* (3), 922–934.
- (3) Guo, R.; Wu, F.; Wang, X.; Bai, Y.; Chuan, W. Multi-Electron Reaction-Boosted High Energy Density Batteries: Material and System Innovation. *J. Electrochem.* **2022**, *28* (12), No. 2219011.
- (4) Murugan, R.; Thangadurai, V.; Weppner, W. Fast lithium ion conduction in garnet-type $\text{Li}_7\text{La}_3\text{Zr}_2\text{O}_{12}$. *Angew. Chem., Int. Ed.* **2007**, *46* (41), 7778–7781.
- (5) Wang, C.; Fu, K.; Kammampata, S. P.; McOwen, D. W.; Samson, A. J.; Zhang, L.; Hitz, G. T.; Nolan, A. M.; Wachsmann, E. D.; Mo, Y.; et al. Garnet-Type Solid-State Electrolytes: Materials, Interfaces, and Batteries. *Chem. Rev.* **2020**, *120* (10), 4257–4300.
- (6) You, Y.; Zhang, D.; Cao, X.; Lü, T.-Y.; Zhu, Z.-Z.; Wu, S. Exploring high-valence element doping in LLZO electrolytes: Effects on phase transition and lithium-ion conductivity. *J. Power Sources* **2024**, *612*, No. 234831.
- (7) Cheng, L.; Chen, W.; Kunz, M.; Persson, K.; Tamura, N.; Chen, G.; Doeff, M. Effect of surface microstructure on electrochemical performance of garnet solid electrolytes. *ACS Appl. Mater. Interfaces* **2015**, *7* (3), 2073–2081.
- (8) Dirican, M.; Yan, C.; Zhu, P.; Zhang, X. Composite solid electrolytes for all-solid-state lithium batteries. *Mater. Sci. Eng. R* **2019**, *136*, 27–46.
- (9) Official Journal of Chinese Society of Electrochemistry. The Top Ten Scientific Questions in Electrochemistry. *J. Electrochem.* **2024**, *30* (1), No. 2024121.
- (10) Krauskopf, T.; Dippel, R.; Hartmann, H.; Peppler, K.; Mogwitz, B.; Richter, F. H.; Zeier, W. G.; Janek, J. Lithium-Metal Growth Kinetics on LLZO Garnet-Type Solid Electrolytes. *Joule* **2019**, *3* (8), 2030–2049.
- (11) Kazyak, E.; Garcia-Mendez, R.; LePage, W. S.; Sharafi, A.; Davis, A. L.; Sanchez, A. J.; Chen, K.-H.; Haslam, C.; Sakamoto, J.; Dasgupta, N. P. Li Penetration in Ceramic Solid Electrolytes: Operando Microscopy Analysis of Morphology, Propagation, and Reversibility. *Matter* **2020**, *2* (4), 1025–1048.
- (12) Han, F.; Westover, A. S.; Yue, J.; Fan, X.; Wang, F.; Chi, M.; Leonard, D. N.; Dudney, N. J.; Wang, H.; Wang, C. High electronic conductivity as the origin of lithium dendrite formation within solid electrolytes. *Nat. Energy* **2019**, *4* (3), 187–196.
- (13) Yu, S.; Siegel, D. J. Grain Boundary Softening: A Potential Mechanism for Lithium Metal Penetration through Stiff Solid Electrolytes. *ACS Appl. Mater. Interfaces* **2018**, *10* (44), 38151–38158.
- (14) Raj, R.; Wolfenstine, J. Current limit diagrams for dendrite formation in solid-state electrolytes for Li-ion batteries. *J. Power Sources* **2017**, *343*, 119–126.
- (15) Sastre, J.; Futscher, M. H.; Pompizi, L.; Aribia, A.; Priebe, A.; Overbeck, J.; Stiefel, M.; Tiwari, A. N.; Romanyuk, Y. E. Blocking lithium dendrite growth in solid-state batteries with an ultrathin amorphous Li-La-Zr-O solid electrolyte. *Commun. Mater.* **2021**, *2* (1), No. 76.
- (16) Huang, Y.; Qin, F.; Dai, K.; Chen, S.; Li, J.; Li, J. Substantial toughening by thick nanoscale amorphous intergranular films in nanocrystalline materials. *J. Appl. Phys.* **2023**, *134* (23), No. 235101.
- (17) Rastogi, P. K.; Duwez, P. Rate of crystallization of an amorphous Fe—P—C alloy. *J. Non-Cryst. Solids* **1970**, *5* (1), 1–16.
- (18) Wu, G.; Chan, K.-C.; Zhu, L.; Sun, L.; Lu, J. Dual-phase nanostructuring as a route to high-strength magnesium alloys. *Nature* **2017**, *545* (7652), 80–83.
- (19) Hayashi, A.; Tatsumisago, M. Invited paper: Recent development of bulk-type solid-state rechargeable lithium batteries with sulfide glass-ceramic electrolytes. *Electron. Mater. Lett.* **2012**, *8* (2), 199–207.
- (20) Song, S.; Qin, X.; Ruan, Y.; Li, W.; Xu, Y.; Zhang, D.; Thokchom, J. Enhanced performance of solid-state lithium-air batteries with continuous 3D garnet network added composite polymer electrolyte. *J. Power Sources* **2020**, *461*, No. 228146.
- (21) Zou, Z.; Li, Y.; Lu, Z.; Wang, D.; Cui, Y.; Guo, B.; Li, Y.; Liang, X.; Feng, J.; Li, H.; et al. Mobile Ions in Composite Solids. *Chem. Rev.* **2020**, *120* (9), 4169–4221.
- (22) You, Y.-W.; Cui, J.; Zhang, X.; Zheng, F.; Wu, S.; Zhu, Z. Properties of lithium phosphorus oxynitride (LiPON) solid electrolyte - Li anode interfaces. *Acta. Phys. Sin.* **2021**, *70* (13), No. 136801.
- (23) Schirmeisen, A.; Taskiran, A.; Fuchs, H.; Bracht, H.; Murugavel, S.; Roling, B. Fast Interfacial Ionic Conduction in Nanostructured Glass Ceramics. *Phys. Rev. Lett.* **2007**, *98* (22), No. 225901.
- (24) Hou, T.; Chen, X.; Jiang, L.; Tang, C. Advances and Atomistic Insights of Electrolytes for Lithium-Ion Batteries and Beyond. *J. Electrochem.* **2022**, *28* (11), No. 2219007.
- (25) Zhang, D.; You, Y.; Zhao, C.; Cao, X.; Lü, T.-Y.; Zhu, Z.-Z.; Wu, S. Influence of Zr aggregation on Li-ion conductivity of amorphous solid-state electrolyte Li—La—Zr—O. *J. Chem. Phys.* **2024**, *160* (11), No. 114701.
- (26) Wang, R.; Dong, Q.; Wang, C.; Hong, M.; Gao, J.; Xie, H.; Guo, M.; Ping, W.; Wang, X.; He, S.; et al. High-Temperature Ultrafast Sintering: Exploiting a New Kinetic Region to Fabricate Porous Solid-State Electrolyte Scaffolds. *Adv. Mater.* **2021**, *33* (34), No. 2100726.
- (27) Wang, C.; Ping, W.; Bai, Q.; Cui, H.; Hensleigh, R.; Wang, R.; Brozena, A. H.; Xu, Z.; Dai, J.; Pei, Y.; et al. A general method to synthesize and sinter bulk ceramics in seconds. *Science* **2020**, *368* (6490), 521–526.
- (28) Liu, J.; You, Y.; Huang, L.; Zheng, Q.; Sun, Z.; Fang, K.; Sha, L.; Liu, M.; Zhan, X.; Zhao, J.; et al. Precisely Tunable Instantaneous Carbon Rearrangement Enables Low-Working-Potential Hard Carbon Toward Sodium-Ion Batteries with Enhanced Energy Density. *Adv. Mater.* **2024**, *36* (44), No. 2407369.
- (29) Huang, L.; You, Y.; Liu, M.; Liu, J.; Gu, J.; Zhan, X.; Wang, W.; Wang, F.; Tan, H.; Wu, S.; Zhang, L. Nanoscale precision welding-enabled quasi-3D conductive carbon blacks for fast-charging and long-lasting secondary batteries. *Carbon* **2024**, *230*, No. 119688.

- (30) Gu, J.; You, Y.; Liu, M.; Huang, L.; Sun, Z.; Liu, J.; Sha, L.; Chen, M.; Li, S.; Wu, S.; et al. Creating rich closed nanopores in anthracite-derived soft carbon enables greatly-enhanced sodium-ion storage in the low-working-voltage region. *Chem. Eng. J.* **2025**, *505*, No. 159331.
- (31) You, Y.; Zheng, F.; Zhang, D.; Zhao, C.; Hu, C.; Cao, X.; Zhu, Z.-z.; Wu, S. Effect of Charge Non-Uniformity on the Lithium Dendrites and Improvement by the LiF Interfacial Layer. *ACS Appl. Energy Mater.* **2022**, *5* (12), 15078–15085.
- (32) Luo, L.; Sun, Z.; You, Y.; Han, X.; Lan, C.; Pei, S.; Su, P.; Zhang, Z.; Li, Y.; Xu, S.; et al. Solid-State Lithium Batteries with Ultrastable Cyclability: An Internal-External Modification Strategy. *ACS Nano* **2024**, *18* (4), 2917–2927.
- (33) Liu, X.; Garcia-Mendez, R.; Lupini, A. R.; Cheng, Y.; Hood, Z. D.; Han, F.; Sharafi, A.; Idrobo, J. C.; Dudney, N. J.; Wang, C.; et al. Local electronic structure variation resulting in Li 'filament' formation within solid electrolytes. *Nat. Mater.* **2021**, *20* (11), 1485–1490.
- (34) Tian, H.-K.; Xu, B.; Qi, Y. Computational study of lithium nucleation tendency in Li₇La₃Zr₂O₁₂ (LLZO) and rational design of interlayer materials to prevent lithium dendrites. *J. Power Sources* **2018**, *392*, 79–86.
- (35) Yu, S.; Schmidt, R. D.; Garcia-Mendez, R.; Herbert, E.; Dudney, N. J.; Wolfenstine, J. B.; Sakamoto, J.; Siegel, D. J. Elastic Properties of the Solid Electrolyte Li₇La₃Zr₂O₁₂ (LLZO). *Chem. Mater.* **2016**, *28* (1), 197–206.
- (36) Gdoutos, E. E. Critical Stress Intensity Factor Fracture Criterion. In *Fracture Mechanics: An Introduction 2020*; Vol. 263, pp 131–165.
- (37) Kresse, G.; Hafner, J. Ab initio molecular dynamics for liquid metals. *Phys. Rev. B* **1993**, *47* (1), 558–561.
- (38) Kresse, G.; Furthmüller, J. Efficient iterative schemes for ab initio total-energy calculations using a plane-wave basis set. *Phys. Rev. B* **1996**, *54* (16), 11169–11186.
- (39) Blöchl, P. E. Projector augmented-wave method. *Phys. Rev. B* **1994**, *50* (24), 17953–17979.
- (40) Perdew, J. P.; Burke, K.; Ernzerhof, M. Generalized gradient approximation made simple. *Phys. Rev. Lett.* **1996**, *77* (18), 3865–3868.
- (41) Andres, J.; Gracia, L.; Gonzalez-Navarrete, P.; Longo, V. M.; Avansi, W., Jr.; Volanti, D. P.; Ferrer, M. M.; Lemos, P. S.; La Porta, F. A.; Hernandez, A. C.; et al. Structural and electronic analysis of the atomic scale nucleation of Ag on alpha-Ag₂WO₄ induced by electron irradiation. *Sci. Rep.* **2014**, *4*, No. 5391.
- (42) Andrés, J.; Gouveia, A. F.; Gracia, L.; Longo, E.; Manzeppi Faccin, G.; da Silva, E. Z.; Pereira, D. H.; San-Miguel, M. A. Formation of Ag nanoparticles under electron beam irradiation: Atomistic origins from first-principles calculations. *Int. J. Quantum Chem.* **2018**, *118* (9), No. 25551.
- (43) Wang, H.; Zhang, L.; Han, J.; E, W. DeePMD-kit: A deep learning package for many-body potential energy representation and molecular dynamics. *Comput. Phys. Commun.* **2018**, *228*, 178–184.
- (44) You, Y.; Zhang, D.; Wu, F.; Cao, X.; Sun, Y.; Zhu, Z.-Z.; Wu, S. Principal component analysis enables the design of deep learning potential precisely capturing LLZO phase transitions. *npj Comput. Mater.* **2024**, *10*, No. 57.
- (45) Zhang, D.; You, Y.; Wu, F.; Cao, X.; Lü, T.-Y.; Sun, Y.; Zhu, Z.-Z.; Wu, S. Exploring the Relationship between Composition and Li-Ion Conductivity in the Amorphous Li–La–Zr–O System. *ACS Materials Lett.* **2024**, *6* (5), 1849–1855.
- (46) Plimpton, S. Fast Parallel Algorithms for Short-Range Molecular Dynamics. *J. Comput. Phys.* **1995**, *117* (1), 1–19.
- (47) Irwin, G. R. Analysis of Stresses and Strains Near the End of a Crack Traversing a Plate. *J. Appl. Mech.* **1957**, *24* (3), 361–364.
- (48) Brochard, L.; Hantal, G.; Laubie, H.; Ulm, F.-J.; Pellenq, R. J. M. Capturing material toughness by molecular simulation: accounting for large yielding effects and limits. *Int. J. Fract.* **2015**, *194* (2), 149–167.
- (49) Hantal, G.; Brochard, L.; Pellenq, R. J.; Ulm, F. J.; Coasne, B. Role of Interfaces in Elasticity and Failure of Clay-Organic Nanocomposites: Toughening upon Interface Weakening? *Langmuir* **2017**, *33* (42), 11457–11466.